catalysts

MDPI

Article

Unravelling the Structural Modification (Meso-Nano-) of Cu/ZnO-Al_2O_3 Catalysts for Methanol Synthesis by the Residual $NaNO_3$ in Hydroxycarbonate Precursors

Rut Guil-López *, Noelia Mota, Jorge Llorente, Elena Millan, Bárbara G. Pawelec, Jose Luis G. Fierro and Rufino M. Navarro *

Instituto de Catálisis y Petroleoquímica, CSIC, C/Marie Curie 2, Cantoblanco, 28049 Madrid, Spain; noelia.mota@icp.csic.es (N.M.); jorge.llorente@csic.es (J.L.); elena.millan.ordonez@csic.es (E.M.); bgarcia@icp.csic.es (B.G.P.); jlgfierro@icp.csic.es (J.L.G.F.)

* Correspondence: rut.guil@icp.csic.es (R.G.-L.); r.navarro@icp.csic.es (R.M.N.)

Received: 23 October 2020; Accepted: 17 November 2020; Published: 19 November 2020

Abstract: The effects of residual $NaNO_3$ on the modification of Cu/ZnO-Al_2O_3 catalysts have been extensively documented, but the modification mechanism is so far unclear. This work studies in detail the influence of the residual sodium nitrate present in the hydroxycarbonate precursors on their decomposition during calcination and how it affects to the formation and configuration of the final active sites of the Cu/ZnO-Al_2O_3 catalysts. Different samples with varying sodium content after washing (from 0.01 to 7.3 wt%) were prepared and studied in detail after calcination and reduction steps. The results of this work demonstrated that $NaNO_3$ affects the decomposition mechanism of the hydroxycarbonate precursors during calcination and produces its decarbonation at low temperature. The enhancement of the decarbonation by $NaNO_3$ leads to segregation and crystallization of CuO and ZnO with loss of mesostructure and surface area in the calcined catalysts. The loss of mesostructure in calcined catalysts affects the subsequent reduction step, decreasing the reducibility and damaging the nanostructure of the reduced catalysts forming large Cu particles in poor contact with ZnO_x that results in a significant decrease in the intrinsic activity of the copper active sites for methanol synthesis.

Keywords: sodium; hydroxycarbonate; copper; catalyst; methanol

1. Introduction

Methanol is one of the most important chemicals used in several industries (global demand exceeds 75 million Mt, 2015) and it is also considered as a promising synthetic transportation fuel which can be obtained from renewable resources [1,2]. Methanol is industrially produced from syngas mixtures ($CO/CO_2/H_2$) at low temperature (230–250 °C) and pressures in the range 50–100 bar over Cu/ZnO/Al_2O_3 catalysts that are considered the most efficient systems for methanol synthesis at low temperature [3–5]. With regard to the Cu/ZnO/Al_2O_3 catalysts, it is known that the presence of well dispersed copper particles in close contact with the partially reduced zinc oxide phase (Cu-ZnO_x synergy) is decisive to obtain catalysts with high activity and stability [6,7]. Therefore, the development of large accessible Cu-ZnO_x contacts is the main objective in the preparation of the Cu/ZnO/Al_2O_3 catalysts [8]. The synthesis method for preparing optimal Cu/ZnO/Al_2O_3 catalysts was developed in the 1960s and includes a multi-step preparation route starting from hydroxycarbonate precursors obtained by coprecipitation of metal nitrates with sodium carbonate, followed by the calcination and reduction steps to generate the active catalysts. The vast literature covering the optimization of the preparation of Cu/ZnO/Al_2O_3 catalysts established that the early stage of synthesis of the hydroxycarbonate precursors is a key step, because the meso- and nanostructure developed by the final catalysts (Cu surface area and Cu-ZnO$_x$ contacts) strongly depends on the nature and structure of these precursors [9,10]. In this way specific phases of copper-zinc hydroxycarbonates, such as zincian malachite [$(Cu,Zn)_2CO_3(OH)_2$] or the amorphous georgeite [$(Cu, Zn)(CO_3)(OH)_2$] are suitable precursors [10–12] because these hydroxycarbonates assure the proper meso- and nanostructure of the catalysts after the calcination and reduction steps. The insertion of Zn into zincian malachite structure favours the nanostructure (high copper dispersion in close contact with Zn) while the amorphous zincian georgeite hydroxycarbonate is responsible of the maintenance of the mesostructure of the catalysts after the calcination. This is because a part of the carbonate structure is retained after calcination (high temperature carbonates, HT-CO_3) which allows achieving high CuO and ZnO interdispersion [11–13]. Therefore, the synthesis of the Cu/ZnO/Al_2O_3 catalysts needs careful control of the preparation parameters during the hydroxycarbonate formation, such as pH, concentration, temperature and ageing time [9–13]. The amount of Na^+ and NO_3^- remaining in the hydroxycarbonate precipitates should be controlled because, as is well documented in the literature [10,13–21], its presence inhibits the interaction and synergetic effect between Cu and ZnOx in the final catalyst leading to low copper metal surface area and catalytic activity. Therefore, in the conventional catalyst preparation by coprecipitation the effective removal of residual Na^+ and NO_3^- is required by repeated washing of the hydroxycarbonate precipitates. In spite of the strong effects of Na^+ and NO_3^- on the structure and activity of the Cu/ZnO catalysts, there is still discussion about how these species are involved in the modification of the meso- and nanostructure of the catalysts after the calcination and reduction steps. In fact, it is not yet clear if the negative effects are caused by the Na^+ or NO_3^- ions and, therefore, different hypotheses to explain the role of Na^+ and NO_3^- have been proposed in the literature [8,13,15–21]. Some studies have shown an increase in the size of CuO and ZnO after calcination of hydroxycarbonates and subsequent reduction because the presence of $NaNO_3$ promotes severe metal agglomeration produced by its exothermic decomposition [13,16,17,19,20]. Other studies proposed that the presence of residual Na^+ produces an inhibitory effect on the substitution of Cu^{2+} by Zn^{2+} in the malachite precursors, thus decreasing the number of Cu-ZnO$_x$ contacts in the final catalysts [15,18]. It is also proposed that high sodium content produces uncontrolled ageing leading to hydroxycarbonates of low surface area [8]. Other proposals indicated that the sodium ions act directly as a poison increasing the surface basicity, by blocking the active copper site sites or by inducing phase separation between the copper and Zn species [21]. Therefore, although the effects of Na^+ and/or NO_3^- are well documented in the literature, the mechanism of modification has not yet been elucidated, in part because the effects have been individually studied on calcination or reduction steps but without evaluating the effect on the entire sequence of steps that configure the meso- and nanostructure of the Cu/ZnO/Al_2O_3 catalysts.

In this work, therefore, we try to shed some light on the fundamental understanding about the effect of $NaNO_3$ on each of the steps (calcination and reduction) involved in the formation and configuration of active sites on the Cu/ZnO-Al_2O_3 catalysts and its relationship with the activity for methanol synthesis from syngas. Evolution of the hydroxycarbonate precursors with different amounts of $NaNO_3$ was studied in deep during calcination and reduction in order to analyse the influence of the Na^+ and/or NO_3^- ions on the meso- and nanostructure of the final Cu/ZnO/Al_2O_3 catalysts.

2. Results and Discussion

2.1. Characterization of Precursors, Calcined and Reduced Catalysts

The amount of sodium in the hydroxycarbonate precursors subjected to the different washing cycles (W/O = precursor without washing and W1, W3 and W3 = precursors after 1, 3 and 6 washing cycles respectively, see materials and methods section) was determined by inductively coupled plasma atomic emission spectroscopy (ICP-AES, Table 1). The amount of sodium in the precipitates without washing was high (7.3 wt%) because it remains strongly adsorbed on the surface of the hydroxycarbonates. This is expected taking into account its role during the crystallization of malachite from georgeite [13]. Considering that the sodium species adsorbed on the hydroxycarbonates are in dynamic equilibrium with the Na ions in the washing solutions its value decreases with the number of washings (Table 1). The loss of Cu and Zn ions in the successive washings was also determined in all cases to be very small (<0.1 wt%). Under our washing conditions, the Na content achieves a minimum value (0.01 wt%) after the third washing cycle.

Table 1. Nomenclature, Na content (inductively coupled plasma atomic emission spectroscopy (ICP-EAS)) and textural properties (form N_2 isotherms) of the hydroxycarbonate precursors.

Sample	**Washing (mL H_2O/g)/Time (min)**	**Na/$NaNO_3$ (wt %)**	**S_{BET} ($m^2 \cdot g^{-1}$) [a]**	**V_{pore} ($cm^3 \cdot g^{-1}$) [a]**
W/O	00	7.339.4	107	0.461
W1	1005	0.502.8	128	0.558
W3	30,015	0.010.05	128	0.578
W6	60,030	0.010.05	127	0.579

[a] per g of hydroxycarbonate

The hydroxycarbonate precursors were studied by X-ray diffraction (XRD, Figure 1) in order to analyse the possible changes in their structure after the different washing cycles. The XRD patterns of all samples showed (Figure 1A) diffraction peaks at 2θ = 14.5°, 17.5°, 24.1°, 32.5° and 35.6° corresponding to the (2 0 2), (1 2 0), (2 2 0), (2 0 1) and (2 1 −1) crystal planes of the zincian malachite structure (Joint Committee on Powder Diffraction Standards, JCPDS, no. 17-0216, $(Cu/Zn)_2CO_3(OH)_2$). The diffraction peaks of the zincian malachite structures are of similar definition and intensity in all precipitates indicating similar crystallinity and size.

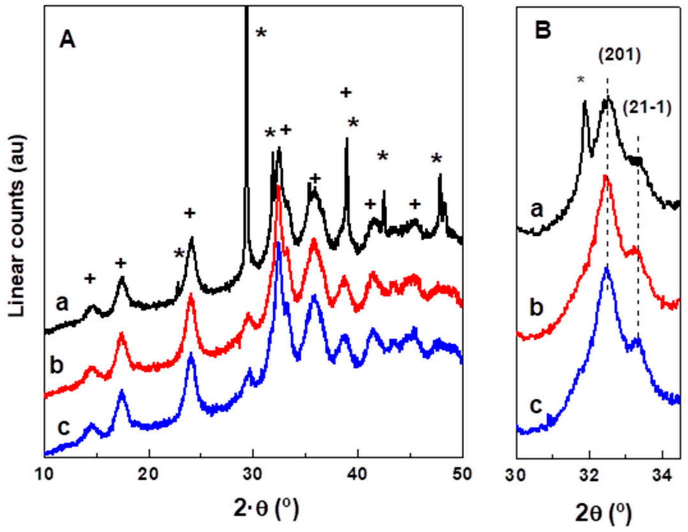

Figure 1. X-ray diffraction (XRD) patterns (**A**) and expansion in the interval 30–35° (**B**) of the hydroxycarbonate precursors: (a) W/O (−), (b) W1 (−), (c) W3 (−) (+ zinzian-malachite ($(Cu/Zn)_2CO_3(OH)_2$, * $NaNO_3$).

The crystalline domain size of the malachite phase calculated from the (2 2 0) plane revealed less than 0.5% of variation in size in all samples after the different washing cycles (Figure 1B). The position of the (2 1 −1) diffraction peak is the same in all precipitates (Figure 1B) suggesting similar Zn insertion in the malachite structure since the position of this reflection is sensitive to changes in the Zn incorporation into the zincian malachite-phase. Therefore, the XRD results seem to indicate that there is no major modification in the crystalline structure of the zincian malachite phases of the precursors after the washing cycles. The unwashed precipitate (W/0) presented additional strong diffraction peaks at

2θ 29.4°, 31.9°, 38.9°, 42.7° and 48.0° corresponding to the (1 0 4), (0 0 6), (1 1 3), (2 0 2), and (0 1 8) crystalline planes of $NaNO_3$ (JCPDS no. 36-1474 Figure 1A). However, the presence of crystalline $NaNO_3$ was not detected in any of the washed precipitates (W1, W3) as consequence of the low content of $NaNO_3$ in the W3 precursor (0.05 wt%) or the high dispersion of $NaNO_3$ in the W1 precursor that produces small crystallites of $NaNO_3$ not detectable by XRD (dp < 4 nm).

The absence of diffraction peaks corresponding to $NaNO_3$ in the W1 precursor indicated the absence of crystallites of $NaNO_3$ detectable through XRD (dp > 2 nm). Obviously the existence of $NaNO_3$ in W1 precursor was confirmed by chemical analysis and, therefore, the absence of diffraction peaks in the W1 precursor indicates the high dispersion of the $NaNO_3$ that produce small crystallites of $NaNO_3$ (dp < 4 nm) not detectable by XRD.

The structure and morphology of the precursors were analyzed by scanning electron microscopy (SEM, Figure 2). SEM micrographs of all precursors show a similar morphology composed by globular particles in combination with distorted rod-like structures. The observed structuration of the precursors is characteristic of the presence of small crystalline zincian malachite (rod like shape) [11] derived from amorphous georgeite (globular shape) [10] in line with the previous XRD patterns which revealed the existence of small crystalline domains of zincian malachite in all precursors. It is well known that the initial structure of precursors with formation of small crystals of zincian malachite is a prerequisite for the formation of porous mesostructures with a highly accessible surface area [11].

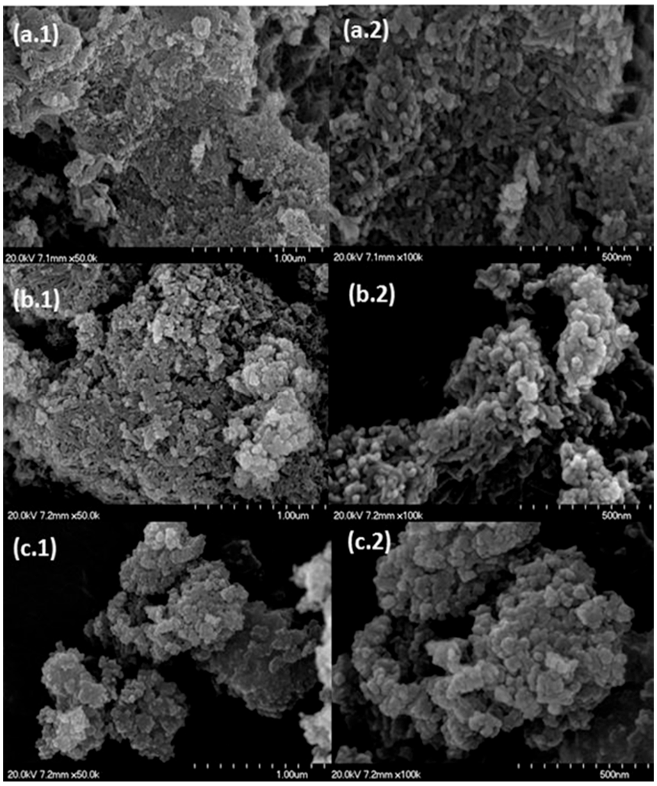

Figure 2. Scanning electron microscope (SEM) micrographs of the hydroxycarbonate precursors (**a**) W/O, (**b**) W1, (**c**) W3 with two magnifications: (1), ×50,000, and (2), ×100,000.

Textural properties of the hydroxycarbonate precursors were derived from N_2 isotherms (Figure S1) and the results are summarized in Table 1. All precipitates presented type IV isotherms with an H2 hysteresis loop (Figure S1) that are characteristic of mesoporous materials with disordered porous structure. Brunauer–Emmett–Teller (BET) surface area and pore volume of the precursors show differences between the unwashed and washed samples (from 107 in the unwashed precipitate to 126–128 $m^2 \cdot g^{-1}$ in washed samples, Table 1) despite the fact that they have similar development of zincian malachite phase (XRD, Figure 1) which, as indicated above, are responsible of the porous mesostructure of the hydroxycarbonate precursors. This result seems to indicate that some of the $NaNO_3$ in the unwashed precipitate partially blocks the porous structure developed by the zincian malachite in the precipitates which is opened after the removal of $NaNO_3$ by washing. In line with this, the BET surface area of precursors does not change significantly after the first washing because most of the $NaNO_3$ was removed during this first washing cycle (Table 1). However the average pore volume of the precipitates slightly increases after the first washing cycle because the successive washing cycles remove the last traces of the $NaNO_3$ inside the pores.

The thermal decomposition of precursors was studied by thermogravimetry (Figure 3A) and analysis of the evolved gases during the decomposition was followed by mass spectrometry (Figure 3B). The overall mass loss of all precursors are close to the expected value (29%) corresponding to the evolution of structural hydroxyl groups and carbonate units from zincian malachite $(Cu/Zn)_2CO_3(OH)_2$). In the case of the unwashed sample an additional mass loss step was observed at T > 650 °C associated with the thermal decomposition of the large amount of $NaNO_3$ [22] present in this sample. The decomposition patterns of the precipitates show distinct mass loss profiles depending on the $NaNO_3$ content after the washing cycles.

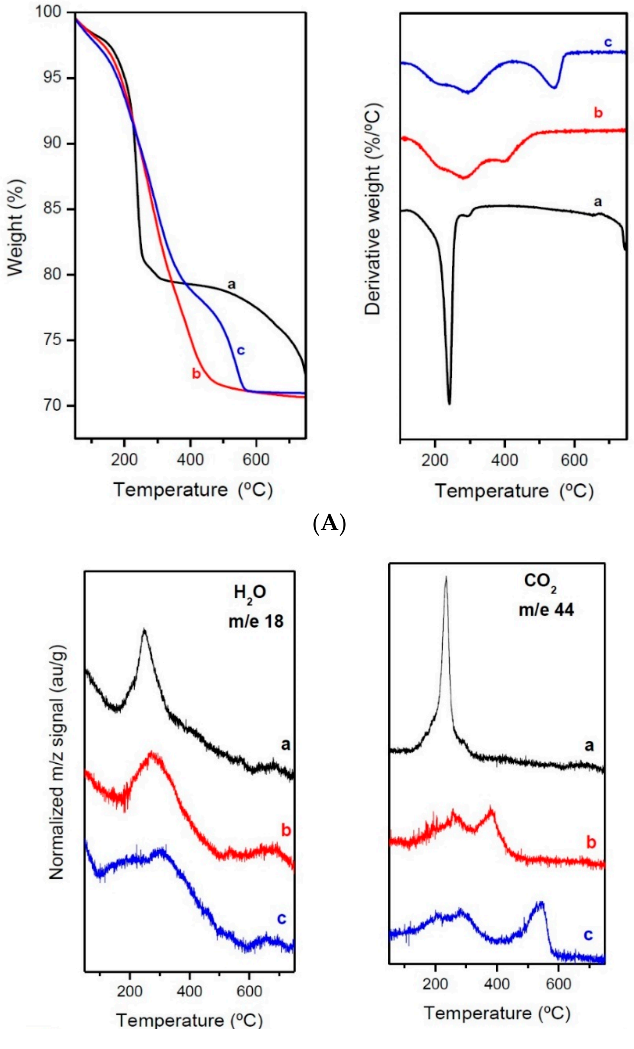

(**A**)

(**B**)

Figure 3. Thermogravimetry/differential thermal analysis (TG/DTA) patterns (**A**) and mass spectrometry (MS) traces (H_2O and CO_2) (**B**) corresponding to the decomposition of the hydroxycarbonate precursors: (a) W/O (–), (b) W1 (–), (c) W3 (–).

The unwashed precipitate (W/O) shows two decomposition steps at low (150–275 °C) and high temperature (600 °C) that correspond to the dehydroxylation and decarbonation of the zinzian malachite hydroxicarbonate in one step (step a 150–275 °C) while the step at high temperature is associated with the decomposition of the large amount of $NaNO_3$ present in this sample. In the case of the W1 precursor it decomposes in two steps at low (150–365 °C) and high temperature (365–520 °C). The decomposition step at low temperature corresponds to the dehydroxylation and partial decarbonation of the zinzian malachite hydroxicarbonate while the second decomposition step at high temperature was associated to the decarbonation of anion-modified mixed metal oxides [23] or a mixture of carbonates and oxides [24] formed from the previous decomposition step. The W3 precursor also shows the decomposition step at low temperature (150–410 °C) that correspond to the dehydroxylation and partial decarbonation of the zinzian malachite hydroxicarbonate while the second decomposition step associated to the decarbonation of the mixture of carbonates and oxides formed from the previous decomposition step shift in this case to higher temperature (410–598 °C, HT-CO_3)). The origin of the decarbonation step at high temperature (HT-CO_3) was not clearly defined in the literature but it has beneficial effect for obtaining highly active catalyst since the residual carbonates after calcination produce good contact and interdispersion of CuO and ZnO leading to high Cu-ZnO synergy in the reduced catalyst [25]. The second decarbonation step of the hydroxicarbonate precursors shifts to lower temperature as the $NaNO_3$ content in the hydroxicarbonate precursors increases, as shown in Figure 3.

In order to investigate the role of the $NaNO_3$ in the decarbonation step of the hydroxicarbonate precursors, an additional thermogravimetric (TG) experiment was carried out in which the decomposition of the precursor with minimum $NaNO_3$ content (after three washing cycles, W3) was mixed (by grinding) with different amounts of $NaNO_3$ (1.8 and 5.0 wt%). The CO_2 evolved during decomposition of the W3 precursor mixed with different amounts of $NaNO_3$ as shown in Figure 4. The data in Figure 4 clearly show that $NaNO_3$ facilitates the decarbonation of the hydroxicarbonate by shifting the second decarbonation step (HT-CO_3) to lower temperature. Additional TG decomposition experiments on the W3 precipitate mixed with other Na^+ and $NO_3{}^-$ salts (NaCl and KNO_3) were performed in order to distinguish the effect of the Na^+ or $NO_3{}^-$ in the decomposition of the high-temperature decarbonation step (HT-CO_3). These results (Table S1) demonstrated that decarbonation of HT-CO_3 in precipitates is facilitated by the presence of alkali metal nitrates such as $NaNO_3$ or KNO_3 and not by the other NaCl salt. To the best of our knowledge, the effect of $NaNO_3$ on the decarbonation of HT-CO_3 during the thermal decomposition of Cu/Zn hydroxycarbonates was only suggested by Bems et al. [26] and it is demonstrated for the first time in this work. This effect may be related to the ability of the alkali metal nitrates to accelerate the decarbonation as already demonstrated in the decomposition of magnesium carbonate and hydroxycarbonates in the presence of $NaNO_3$ [27,28]. Few mechanisms have proposed in the literature an explanation for the effect of $NaNO_3$ on decarbonation, but in all of them the molten $NaNO_3$ facilitates the decarbonation, providing a liquid channel that promotes both the release of CO_2 and the oxide crystallization from the carbonates [29,30]. A similar mechanism could, therefore, be proposed in our case to justify the decarbonation at lower temperature by the presence of $NaNO_3$ observed in the Cu/Zn hydroxycarbonate precursors.

According to the TGA profile (Figure 3), the W/O, W1 and W3 precursors were calcined at 260, 310 and 360 °C, respectively, to decompose the hydroxycarbonates and to form the copper and zinc oxides in the calcined catalysts. The XRD profiles of calcined CuO/ZnO-Al catalysts (Figure 5) clearly show the impact of the residual $NaNO_3$ on the crystallization of the copper and zinc oxides after the decomposition of the precursors. The calcined catalyst derived from the precursor with minimum $NaNO_3$ content (CuO/ZnO-Al-W3) shows broad and poorly defined diffraction peaks of ZnO (JCPDS: 43-002) without any detectable peaks corresponding to CuO (JCPDS: 1-117) that demonstrated the absence of crystallization of CuO and the good interdispersion with ZnO. On the contrary, a significant increase in the segregation and crystallization of CuO and ZnO was observed on the calcined catalysts derived from precursors with residual $NaNO_3$. The size of CuO crystallites in the calcined catalysts increases (Table 2) as the $NaNO_3$ content in the precursors from which they derive increases (Table 1).

Going from the calcined catalyst derived from the unwashed precursor (CuO/ZnO-Al-W/O) to the catalyst derived from the precursor after three washing cycles (CuO/ZnO-Al-W3), the CuO crystallite size decreases from 9 nm to a value lower than 2 nm (Table 2).

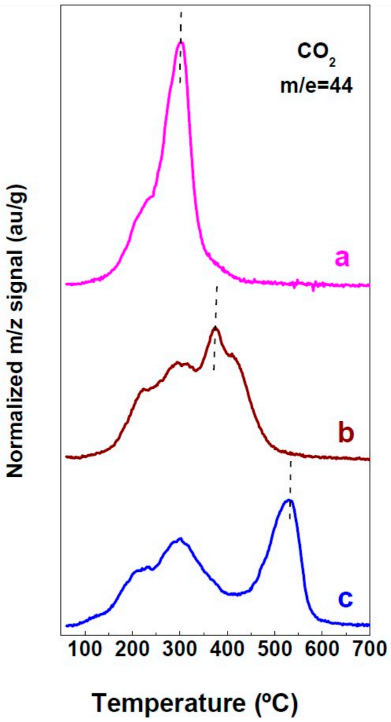

Figure 4. MS CO_2 traces corresponding to decomposition of W3 hydroxycarbonate precursor mixed with different amount of $NaNO_3$ (**a**) +5.0 wt% $NaNO_3$ (–) (**b**) +1.8 wt% $NaNO_3$ (–), (**c**) as original, no $NaNO_3$ added (–).

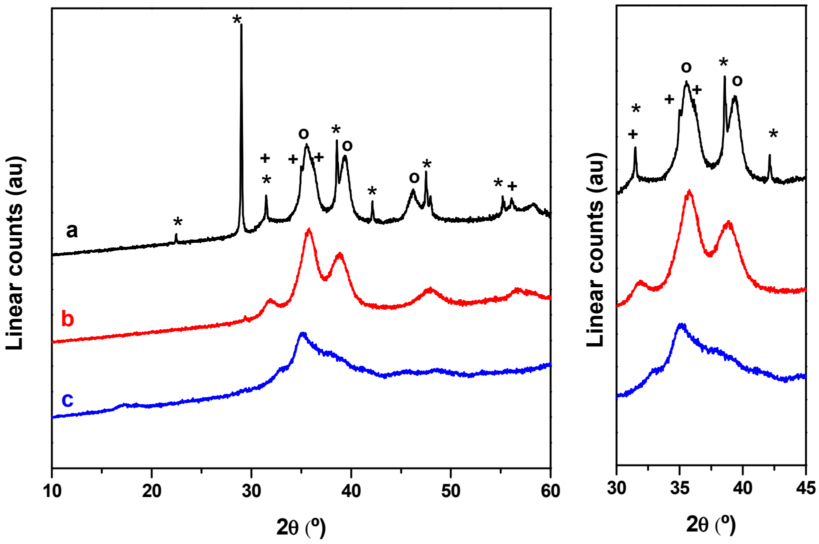

Figure 5. XRD profiles of calcined catalysts derived from hydroxycarbonate precursors: (**a**) CuO/ZnO-Al-W/O (–), (**b**) CuO/ZnO-Al-W1 (–), (**c**) CuO/ZnO-Al-W3 (–) (o CuO, + ZnO, * $NaNO_3$).

Table 2. CuO crystallite size (XRD), carbonate retention (thermogravimetric analysis (TGA)), surface area and reduction temperature (from temperature programmed reduction, TPR) of calcined catalysts.

Catalyst	d_p CuO (nm)	HT-CO_3 T (°C)-wt%	S_{BET} [(a)] (m^2/g)	TPR T (°C)
CuO/ZnO-Al-W/O	9	-	67.1	265
CuO/ZnO-Al W1	5	386–2.6	87.5	195
CuO/ZnO-Al W3	<2	528–8.5	107	165

(a) per g of CuO/ZnO-Al.

Other studies in the literature have already shown the adverse effect of $NaNO_3$ on the CuO and ZnO after calcination of hydroxycarbonate precursors but there is limited understanding of the effect of $NaNO_3$ on the growth of the Cu and Zn oxides during the calcination [17,26]. It is well known than the presence of residual carbonates after decomposition of the precursors is beneficial to obtain small CuO and ZnO particles finely interdispersed in the calcined catalysts [23–25]. The role of the residual carbonates on the dispersion of the oxide particles is still unclear but it is suggested that they serve as growth inhibitors for the oxide crystallites or that they act as binders that separates the oxide particles [25]. In line with this, the carbonate retention on calcined CuO/ZnO-Al catalysts determined by TGA (Table 2) shows a clear parallelism between the residual carbonates after calcination and the growth of CuO and ZnO on the calcined catalysts. The residual carbonates on calcined catalyst are related to the decarbonation step at high temperature of the precursors (HT-CO_3) so that the precursors with HT-CO_3 will give rise to residual carbonates on calcined catalysts that inhibit the CuO and ZnO oxide growth. The CO_2 evolved during the decomposition of precursors (Figures 3 and 4) clearly shows that $NaNO_3$ facilitates the decarbonation of the precursors, shifting the decomposition of the HT-CO_3 to lower temperature. The ability of $NaNO_3$ to facilitate the decarbonation is probably related with the fact that molten $NaNO_3$ provides a liquid channel that promotes the release of CO_2 from the precursors [29,30]. Therefore the crystalline growth of CuO and ZnO in calcined catalysts derived from precursors with $NaNO_3$ could be due to the loss of the residual carbonates that act as inhibitors/binders as consequence of the ability of $NaNO_3$ to accelerate the decarbonation of the HT-CO3 in the precursors. In addition to that, the growth of CuO/ZnO could also be related with the ability of the molten $NaNO_3$ to promote the rapid crystallization of metal oxides, as was already described in the case of MgO which shows higher crystallinity and size after decarbonation of magnesium carbonate and hydroxycarbonate in contact with $NaNO_3$ [29].

The observed differences in the thermal decomposition of precursors obviously influence on the mesostructure of the formed calcined catalysts. The calcined catalyst derived from the W3 precursor shows a surface BET area (CuO/ZnO-Al-W3 = 107 $m^2 \cdot g^{-1}$, Table 2) similar to the area developed by the precursor (W3 = 128 $m^2 \cdot g^{-1}$, Table 1). By contrast, the calcined catalysts derived from the W/O and W1 precursors show a significant loss in their BET surface area (CuO/ZnO-Al-W/O = 67.1 $m^2 \cdot g^{-1}$, CuO/ZnO-Al-W-1 = 87.5 $m^2 \cdot g^{-1}$, Table 2) respect to that developed by their precursors (W/O = 107 $m^2 \cdot g^{-1}$; W1 = 128 $m^2 \cdot g^{-1}$ Table 1). Therefore the calcined catalysts formed after decomposition of precursors develop less mesostructure and surface area as the $NaNO_3$ content in the precursors increases. It has been widely reported in the literature [31–33] that the carbonate retention after calcination determines the mesostructure of calcined catalysts because as discussed above, they inhibit the macro-crystalline growth of CuO/ZnO avoiding its macro-phase segregated agglomeration. Therefore, the results of this work illustrate that the presence of $NaNO_3$ modifies the mesostructure of the calcined catalysts because it enhances the decomposition of HT-CO_3 during calcination which produces macro-crystalline CuO/ZnO agglomerates with loss of mesostructure and surface area. The decomposition of HT-CO_3 during calcination depends on the $NaNO_3$ content as demonstrated in Figure 4 and, therefore, the growth of CuO/ZnO and loss of surface area in calcined catalysts decreases as the nitrate content in precursor increases.

The reducibility of the calcined catalysts was investigated by temperature programmed reduction (Figure 6). The temperature programmed reduction (TPR) profile of the catalyst with minimum nitrate content (CuO/ZnO-Al-W3) shows a sharp reduction peak at 165 °C preceded by a small shoulder at lower temperature. According to the general interpretation, the main reduction peak is typical of the reduction of small CuO nanoparticles highly dispersed in contact with ZnO [34,35] while the shoulder at low temperature is probably related to the reduction of finely dispersed CuO [36] or to the remaining carbonate species [37]. The latter option seems more likely because the gas analysis by mass spectrometry detected the reduction with simultaneous formation of CO_2. The calcined catalysts derived from precursors with residual nitrate (CuO/ZnO-Al-W/O and CuO/ZnO-Al-W1) show lower reducibility as consequence of their crystalline CuO and ZnO growth. The reduction temperature on these samples shifts to higher values as the dispersed CuO nanoparticles in contact with ZnO decreases in accordance with the growth and segregation observed by XRD (Figure 5). In the case of the catalyst with the highest nitrate content (CuO/ZnO-Al-W/O, Figure 6c) its reduction starts at 265 °C, which is close to that reported for bulk CuO particles. The reduction peak includes an additional sharp peak at 330 °C that corresponds to the reduction of the $NaNO_3$, corroborated by the NH_3 formation observed by mass spectrometry. The reduction of $NaNO_3$ is produced by the spillover of hydrogen on the reduced metallic copper atoms [38].

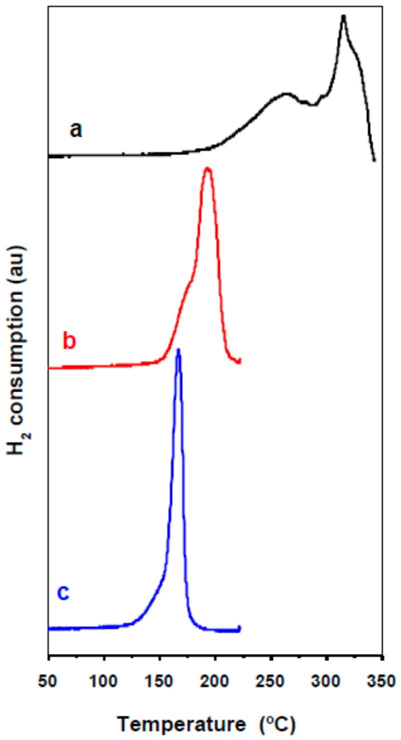

Figure 6. Temperature programmed reduction profiles of calcined catalysts: (**a**) CuO/ZnO-Al-W/O (−), (**b**) CuO/ZnO-Al-W1 (−), (**c**) CuO/ZnO-Al-W3 (−).

Since the size of the CuO crystallites and its interaction with ZnO particles in the calcined catalysts define the reducibility and the corresponding size of Cu^0 nanoparticles, the nanostructure of the reduced catalysts was studied by transmission electron microscopy (TEM, Figure 7) and N_2O chemisorption (Table 3).

The reduced catalyst derived from precursor with minimum nitrate content (Cu/ZnO-Al-W3) shows aggregates of small particles formed by metallic copper with an average size of 7–8 nm homogeneously distributed and in close contact, partially covered, with ZnO (Figure 7c) forming the typical nanostructuration observed for highly active methanol synthesis catalysts [39]. By contrast, the reduced catalysts derived from precursors with residual nitrate (Figure 7a,b) show higher metallic copper nanoparticles (9–10 nm for Cu/ZnO-Al-W1 and 20 nm for Cu/ZnO-Al-W/O) segregated from large ZnO particles in accordance with the growth of CuO and ZnO observed in their calcined precursors. However, the growth and segregation of metallic copper particles is especially significant in the case of the sample with the higher $NaNO_3$ content (Cu/ZnO-Al-W/O) and points out that in addition to the growth of CuO crystallites in the calcined catalyst, the local exothermicity generated by the reduction of the residual nitrate (Figure 6a) could also facilitate the migration and coalescence of the copper particles during reduction resulting in the observed strong Cu growth [40]. Obviously the Cu-ZnO synergy on reduced catalysts is affected by the above commented changes in the nanostructuration of metallic Cu and ZnO observed by TEM.

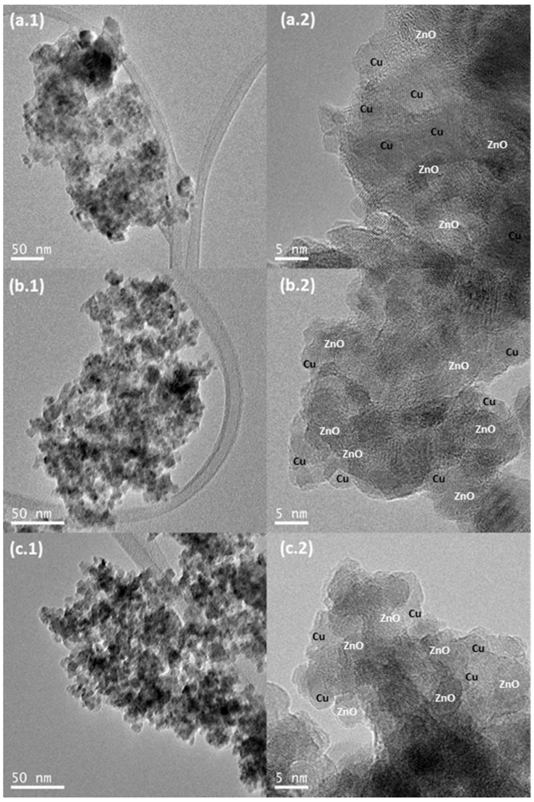

Figure 7. Transmission electron microscopy (TEM) micrographs of reduced catalysts: (**a.1**,**a.2**) Cu/ZnO-Al-W/O, (**b.1**,**b.2**) Cu/ZnOAl-W1, (**c.1**,**c.2**) Cu/ZnO-Al-W3.

Table 3. Effective Cu surface area (N_2O chemisorption) and activity data in methanol synthesis from syngas (initial methanol yield, TOF (turnover overall frequency) and deactivation rate (decay in umol CH_3OH/min gcat) of reduced catalysts.

Catalyst	Effective Cu Surface Area ($m^2 \cdot g^{-1}$)	Initial CH_3OH Time Yield [a] (μmol $min^{-1} \cdot g^{-1}$)	TOF [b] (s^{-1})	Deactivation Rate (μmol $min^{-1} \cdot g^{-1}$)
Cu/ZnO-Al W/O	0	0	-	-
Cu/ZnO-Al W1	29.1	300	7.0	0.05
Cu/ZnO-Al W3	41.3	1050	17.3	0.01

[a] initial activity at $t = 0.5$ h; [b] TOF = $\mu mol_{CH3OH}\ \mu mol_{Cu(surface)}{}^{-1} \cdot s^{-1}$.

The Cu-ZnO synergy were determined by N_2O chemisorption because in addition to the measurement of the copper surface area, the N_2O chemisorption also tritates the contacts with defective ZnO_x species [41]. Therefore, the Cu-ZnO synergy determined from N_2O chemisorption can be used as a rough indicator for methanol synthesis activity. The N_2O chemisorption data on reduced catalysts (Table 3) show differences in accordance with the copper dispersion and contacts of the Cu nanoparticles with ZnO/ZnO_x species previously observed by TEM. Thus the reduced catalyst derived from the precursor with low nitrate content (Cu/ZnO-Al-W3) shows a very high value of specific Cu surface area (41.3 $m^2 \cdot g^{-1}$) in line with the small Cu nanoparticles in close contact with ZnO shown in their TEM images (Figure 7(c.2)). By contrast, the catalysts derived from precursors with residual nitrate (CuO/ZnO-Al-W/O and CuO/ZnO-Al-W1) show lower values of specific Cu surface area in accordance with the growth and segregation of the copper species observed on the TEM images of the samples (Figure 7(a.2,b.2)). It should be noted that the catalyst derived from the high-nitrate precursor (Cu/ZnO-Al-W/O) does not show any N_2O chemisorption capacity that means small copper surface area and absence of Cu-ZnO synergy. This fact is a consequence of the formation of large Cu crystallites segregated from the ZnO particles existing in this sample and derived from the macro-crystalline growth of CuO and ZnO after calcination and the strong Cu growth after reduction produced by the local exothermicity generated by the reduction of the residual nitrate.

2.2. Activity in Methanol Synthesis

The catalysts were tested in the synthesis of methanol from syngas and the activity data were presented in Figure 8 and collected in Table 3. As expected, the changes observed in the nanostructure, crystallization and segregation of Cu and ZnO in the reduced catalysts caused by the $NaNO_3$ in precipitates produce very significant changes in their activity for methanol synthesis. The catalyst derived from the precipitate without washing (with maximum $NaNO_3$ content, Cu/ZnO-Al W/O) was ineffective for methanol synthesis. This behaviour could be correlated with the small copper surface area and absence of Cu-ZnO synergy (Table 3) derived from the large Cu crystallites with poor contacts with ZnO observed in this reduced catalyst (Figure 7(a.2)). The methanol activity of catalysts derived from washed precursors (Cu/ZnO-Al W1 and Cu/ZnO-Al W3) increase with decreasing residual $NaNO_3$ content in the samples, displaying the catalyst with minimum nitrate content (Cu/ZnO-Al W3) a very high performance in methanol synthesis (1050 μmol_{CH3OH} $min^{-1} \cdot g_{cat}{}^{-1}$) that decreases by more than a third in the case of the sample Cu/ZnO-Al W1 (300 μmol_{CH3OH} $min^{-1} \cdot g_{cat}{}^{-1}$). Higher stability is also observed for the catalyst Cu/ZnO-Al W3 that show a more stable methanol production compared to the slight decay observed for the Cu/ZnO-Al W1 sample with residual sodium nitrate (Table 3).

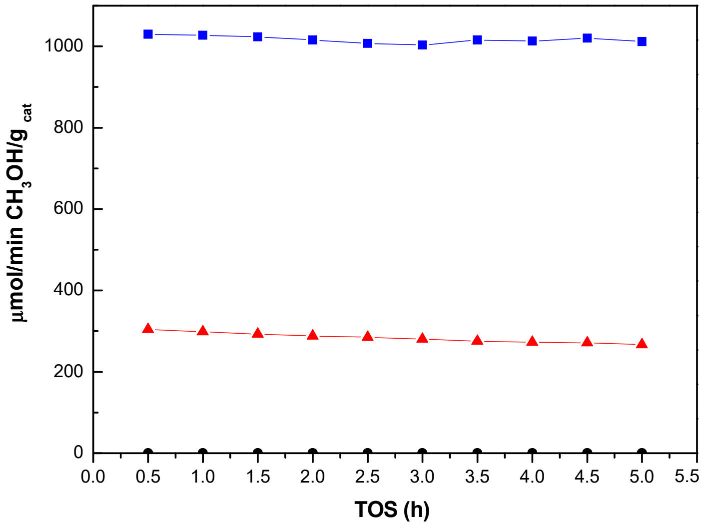

Figure 8. Activity measurements in methanol synthesis from syngas vs. time on stream (TOS) (250 °C, P = 3 MPa, GHSV (gas hourly space velocity) = 32,700 h^{-1}) over: (●) Cu/ZnO-Al-W/O, (▲) Cu/ZnO-Al-W1, (■) Cu/ZnO-Al-W3.

It is well known that the activity of methanol synthesis within families of Cu-ZnO catalysts prepared by the same methodology is correlated with the copper surface area and Cu-ZnO synergy determined by N_2O chemisorption. However, the intrinsic activity of catalysts calculated with respect to Cu surface areas (TOF in Table 3) shows an important difference between the samples derived from washed precursors with different $NaNO_3$ content, dropping by more than half in the case of the Cu/ZnO-Al W1 catalyst (7.0 s^{-1}) respect to the catalyst with the lowest nitrate content Cu/ZnO-Al W3 (17.3 s^{-1}).

As indicated previously the activity of copper catalysts strongly depends on the Cu-ZnO synergy that defines the nature of the active site which, although still under debate, is related to the close contact of Cu and reduced ZnO species: Cu^0–Zn^0 surface alloy [42], $Zn^{\delta+}$ species at the defective Cu^0 surface [8] or graphitic-like ZnO_x layer on Cu^0 [43]. Therefore, the difference in the intrinsic activities observed between the washed Cu/ZnO-Al-W1 and Cu/ZnO-Al W3 catalysts is a clear indication of the change in the nature of the active sites in the sample derived from precursors containing $NaNO_3$. Regardless of the active site model, to obtain high active sites in Cu-ZnO-Al catalysts it is necessary to start from mesostructured calcined catalysts which contain finely interdispersed CuO and ZnO nanoparticles with improved reducibility that facilitates the formation, after reduction, of small Cu nanoparticles homogeneously distributed and in intimate contact with partially reduced ZnO_x entities (strong metal-support interaction). This is the case of the calcined precursor derived from the precipitate with low nitrate content (Cu/ZnO-Al W3) that displays small CuO nanoparticles highly dispersed in contact with ZnO (Figure 5c) mesostructured and stabilized by residual carbonates that allows the reduction at low temperature with the formation of small Cu particles in close contact with ZnO (ZnO_x) nanoparticles (Figure 7(c.1,c.2)). By contrast, the significant increase in the segregation and crystallization of CuO and ZnO produced by the decomposition of HT-CO_3 promoted by the presence of $NaNO_3$ in the calcined CuO/ZnO-Al W1 precursor (Figure 5b) leads to lower reducibility and larger Cu particles with poorer contact with ZnO (Figure 7(b.1,b.2)) which explains the lower intrinsic activity of the active sites of this catalyst by loss of the nanostructuration in the contact of Cu with the reduced ZnO species.

Summarizing, the results presented in this work shows that residual $NaNO_3$ on precipitates first produces the loss of the mesostructuration in the calcined catalysts. The modification in the mesostructuration of the calcined catalysts depends on the $NaNO_3$ content and it affects their subsequent evolution after reduction producing large Cu particles in poor contact with ZnO_x which translates into active sites with poor intrinsic activity. The loss of the mesostructuration in the calcined catalysts was investigated in detail and it was demonstrated for the first time that is related with the decarbonation of the hydroxycarbonates at low temperature mediated by the presence of $NaNO_3$.

3. Materials and Methods

3.1. Catalysts' Preparation

The hydroxycarbonate precursors were prepared by co-precipitation of $Cu^{2+}/Zn^{2+}/Al^{3+}$ ions using the optimized coprecipitation method developed by Schuman et al. to obtain highly active catalysts [44]. The atomic composition of the precursors (68:29:3 Cu:Zn:Al) was chosen to achieve the optimal incorporation of Zn into the Cu-malachite hydroxycarbonate precursor with the maximum promoting effect of the Al-dopant [45]. The hydroxycarbonate precursor was precipitated at constant pH (6.5) and temperature (65 °C) under continuous stirring using 1 M solutions of the nitrate salts of Cu ($Cu(NO_3)_2 \cdot 2.5H_2O$, Sigma-Aldrich >98%), Zn ($Zn[(NO_3)_2 \cdot 6H_2O$, Sigma-Aldrich >99%), and Al ($Al(NO_3)_2 \cdot 9H_2O$, Sigma-Aldrich >99%) and 1.6 M solution of sodium carbonate ($Na_2CO_3 \cdot 10H_2O$, Panreac AppliChem for Analysis) as precipitating agent. The initial precipitate was amorphous in the form of georgeite. However, after 30 min of aging, there was a decrease in pH related to the transformation of the amorphous georgeite into the crystalline malachite [9]. This transformation was associated with a change in the colour of the precipitates from the blue of the georgeite to the greenish of the malachite. Once the change in colour occurred, the precipitate was additionally aged for another 15 min to assure the complete crystallization of the malachite precipitate. The aged precipitate was filtered to separate the precipitate from the mother liquor. An aliquot of the precipitate was isolated as a sample without washing treatment (W/O sample). The rest of the precipitate was washed under stirring (500 rpm) with miliQ water (100 mL/$g_{precipitate}$) for 5 min. The solid was filtered after this first washing treatment and an aliquot of the washed solid was isolated (W1 sample). The rest of the precipitate was subjected to five additional washing cycles under stirring (500 rpm) with miliQ water (100 mL/$g_{precipitate}$ for 5 min) and taking samples after 3 (W3 sample) and 6 (W6 sample) washing cycles. After washing, the precipitates were dried at 70 °C for 12 h. Table 1 shows the nomenclature and characteristics of the precipitates subjected to different washing cycles used in this study. Dried hydroxycarbonate precursors were calcined under static air for 2 h (heating rate of 2 $°C·min^{-1}$) to maintain in each calcined catalyst the optimal quantity of residual high temperature carbonates (HT-CO_3). According to the TGA profile (Figure 3), the W/O, W1 and W3 precursors were calcined at 260, 310 and 360 °C, respectively, to decompose the hydroxycarbonates and to form the copper and zinc oxides in the calcined catalysts. Calcined samples were reduced in order to obtain the Cu/ZnO-Al_2O_3 catalysts in their activated form. The activation consists in a thermal treatment under H_2/Ar flow (2.2 vol. %, 50 $mL·min^{-1}$) following the temperature program: RT→(2 $°C·min^{-1}$)→150 °C→(1 $°C·min^{-1}$)→200 °C (2 h).

3.2. Catalysts Characterization

The Na content on hydroxycarbonate precursors was determined by ICP-AES in an ICP-AES Optima 3300 DV Perkin Elmer spectrometer with an Echelle net combined with SC (scintillation counter) detectors.

The crystalline structure of the hydroxycarbonate precursors, calcined and reduced catalysts were determined by XRD using a polycrystal X-ray diffractometer X'Pert Pro with X'Celerator detector from PANalytical (Malvern, Worcs, UK). Each sample was measured in quantitative mode using CuKα radiation (λ = 1.5406 Å, 45 kV and 40 mA), with a 0.04 step size and an accumulation time of 50 s/step. Identification of the phases was achieved by comparison with the JCPDS diffraction data file. Zinc-malachite and CuO average crystal sizes were calculated from the characteristic reflection peaks of the (2 2 0) and (1 1 1) planes, respectively, using the Debye-Scherrer equation.

Textural properties of the hydroxycarbonate precursors and calcined catalysts were obtained from the N_2 adsorption/desorption isotherms measured at −196 °C. The measurements were carried out in automatic ASAP 2420 equipment (Micromeritics, Norcross, GA, USA) after the degassing of the samples at 120 °C for 12 h. The specific surface area (S_{BET}) was calculated by the Brunauer–Emmett–Teller (BET) method. The pore volume (V_{pore}) and the average pore size distribution (D_{pore}) were calculated from desorption data by the Barrett–Joyner–Halenda (BJH) method.

Thermo-gravimetric analysis (TGA) was used to determine the weight loss of the precipitates and calcined catalysts during their thermal treatment in air. The TGA experiments were carried out in a TGA/SDTA 851e balance (Mettler Toledo, Columbus, OH, USA). Samples were placed into an Al-ceramic reactor under 25 mL/min of a 20 vol.% O_2/N_2 gas flow and heated from 40 °C to 600 °C at 10 °C/min heating rate. Analysis of the evolved gases during the thermal treatment of the precipitates in air was followed by mass spectrometry (MS). The sample (20 mg) was placed in a U-shape quartz reactor (4.0 mm ID) and heated from 40 °C up to 600 °C with heating ramp of 10 °C/min under O_2/Ar flow (20 vol.%, 38 mL/min). The evolved gases were analysed online using a Baltzer Prisma QMS 200TM mass spectrometer (Pfeiffer Vacuum, Asslar, Germany) with a quadrupole detector. The studied m/z signals (H_2O, CO, CO_2, NO, NO_2, N_2O and Ar) were normalized with respect to the Ar signal to avoid the changes in the chamber pressure. Analysis of the morphology of the particles present in the precipitates and calcined catalysts were carried out by emission scanning electron microscopy (SEM) in a FE-SEM Hitachi S-4700 cold cathode field emission microscope.

Nanomorphology of the particles in the reduced catalysts were studied by transmission and high-resolution transmission electron microscopy (TEM and HRTEM, respectively) in a TEM/STEM

JEOL 2100F microscope (JEOL, Tokio, Japan) with a field emission gun (FEG) which operates at 200 kV of accelerating voltage.

Reducibility of the calcined catalysts was studied by hydrogen temperature programmed reduction (H_2-TPR). TPR experiments were carried out in semi-automatic equipment (PID Eng and Tech, Micromeritics, Norcross, GA, USA) with a thermal conductivity detector (TCD). 30 mg of calcined sample was placed into a U-shaped quartz reactor (4.0 mm ID) and heated from 25 up to 300 °C with a heating rate of 10 $°C \cdot min^{-1}$ under H_2/Ar flow (10 vol.%, 50 $mL \cdot min^{-1}$).

N_2O chemisorption experiments on the reduced catalysts were carried out to calculate the Cu-surface area using the same equipment employed for TPR experiments. Reduced catalysts (30 mg) were treated with 7.5 $mL \cdot min^{-1}$ of 2 vol.% N_2O/Ar at 25 °C for 5 s. Physisorbed N_2O was removed with 30 $mL \cdot min^{-1}$ of He flow for 30 min. Then, the N_2O passivated catalysts were re-reduced with 50 mL/min of H_2/Ar (10 vol.%) from 25 °C up to 280 °C (heating rate of 10 $°C \cdot min^{-1}$). The amount of hydrogen consumed during the re-reduction was equivalent to the amount of N_2O chemisorbed. The surface of exposed Cu is calculated from the N_2O chemisorption stoichiometry ($Cu/N_2O = 2$) and the value of $1.47 \cdot 10^{19}$ at Cu/m^2 for the mean surface Cu atom density [46].

3.3. Catalytic Activity Tests

The catalytic methanol synthesis reaction was carried out in a stainless steel continuous flow fixed-bed reactor (8.9 mm internal diameter (ID)). Catalytic bed consisted on 200 mg of calcined catalysts diluted with SiC (1:3 vol.) to avoid temperature gradients. Calcined precursors were reduced under H_2/Ar flow (2.21 vol.%, 50 $mL \cdot min^{-1}$) at 200 °C for 2 h. The reactor was fed with 75 mL/min of syngas (vol.%, 4.5% CO_2, 22.0% CO, 58.8% H_2 and 14.7% N_2) and the methanol synthesis rate was measured under a total pressure of 3 MPa at 250 °C for 8 h. The catalytic tests were conducted under high gas hourly space velocity (GHSV) to achieve low conversions to exclude the effect of equilibrium and to better visualize the differences between the samples. Analysis of reaction products was accomplished on-line by gas chromatography using a Varian 450-GC equipment with TCD and a QS-bond column (for CO_2, CH_3OH and H_2O) and a molecular sieve 5A capillary column (for H_2, O_2, N_2, and CO). Activity data are presented as CH_3OH production rate normalized to the weight of calcined precursor loaded in the reactor ($\mu mol_{CH3OH} \cdot min^{-1} \cdot g_{cat}{}^{-1}$).

4. Conclusions

The effect of residual $NaNO_3$ on hydroxycarbonate precipitates on the formation and configuration of active sites on the Cu/ZnO catalysts has been studied. Evolution of the hydroxycarbonates during calcination was studied in depth in order to analyse the effect of residual $NaNO_3$ on the mesostructuration and CuO/ZnO interdispersion. The results show that residual $NaNO_3$ on precipitates strongly affects their transformation into calcined catalyst destroying the mesostructuration and producing segregation and crystallization of CuO and ZnO, more pronounced as the $NaNO_3$ content in the hydroxycarbonates increases. This fact is related to the decarbonation of the HT-carbonates facilitated by the $NaNO_3$, which is described for the first time in this work. It is proposed that molten $NaNO_3$ facilitates the decarbonation providing a liquid channel that promotes both the release of CO_2 and the oxide crystallization from carbonates. The loss of mesostructuration in calcined catalysts affects the subsequent reduction step, decreasing the reducibility and altering the nanostructuration of the reduced catalyst forming large Cu particles in poor contact with ZnO_x. The loss of meso- and nanostructuration depends on the $NaNO_3$ content and become more pronounced as the $NaNO_3$ content increases. In the case of high $NaNO_3$ content, the shift in the reduction temperature is such that reduction also includes the reduction of the residual nitrate creating local exothermicity that produces the migration and coalescence of the copper particles resulting in strong Cu growth. The changes in the meso- and nanostructure of the reduced catalysts caused by the $NaNO_3$ produce a decrease in their activity for methanol synthesis with an absolute lack of activity in the case of the catalyst with high $NaNO_3$ content as befits its large Cu crystallites with poor contacts with ZnO.

Supplementary Materials: The following are available online at http://www.mdpi.com/2073-4344/10/11/1346/s1, Figure S1: N2 adsorption/desorption isotherms (A) and pore size distribution (B) of the hydroxycarbonate precursors: (a) W/O (–), (b) W1 (–), (c) W3 (–), (d) W6 (–), Table S1. Effect of Na^+ and NO_3^- salts (1.8 wt%) on the decarbonation step at high temperature of the W3 hydroxicarbonate precursor.

Author Contributions: Conceptualization, R.M.N.; Formal analysis, N.M., J.L.G.F. and R.M.N.; Investigation, R.G.-L., N.M., J.L., E.M., B.G.P. and J.L.G.F.; Methodology, R.G.-L., J.L.G.F. and R.M.N.; Writing—original draft, R.G.-L. and R.M.N.; Writing—review and editing, R.G.-L., N.M., B.G.P. and R.M.N. All authors have read and agreed to the published version of the manuscript.

Funding: The present investigation was performed within the research programs CTQ2016-76505-C3-1 and PID2019-111219RB-100 supported by the Spanish Ministry of Science, Innovation and Universities. The Autonomous Community of Madrid is also gratefully acknowledged for funding BIOTRES-CM (P2018/EMT-4344) project. Elena Millán would like to acknowledge the FPI programme from the Spanish Ministry of Science, Innovation and Universities for the research grant.

Conflicts of Interest: The authors declare no conflict of interest. The funders had no role in the design of the study; in the collection, analyses, or interpretation of data; in the writing of the manuscript; or in the decision to publish the results.

References

1. Olah, G.A. Towards oil independence through renewable methanol chemistry. *Angew. Chem. Int. Ed.* **2013**, *52*, 104–107. [CrossRef] [PubMed]
2. Smit, B. Carbon Capture and Storage: Introductory Lecture. *Faraday Discuss.* **2016**, *192*, 9–25. [CrossRef] [PubMed]
3. Melian-Cabrera, I.; Lopez-Granados, M.; Fierro, J.L.G. Pd-Modified Cu–Zn Catalysts for Methanol Synthesis from CO_2/H_2 Mixtures: Catalytic Structures and Performance. *J. Catal.* **2002**, *210*, 285–294. [CrossRef]
4. Klier, K. Methanol synthesis. *Adv. Catal.* **1982**, *31*, 243–313. [CrossRef]
5. Fichtl, M.B.; Schlereth, D.; Jacobsen, N.; Kasatkin, I.; Schumann, J.; Behrens, M.; Schlögl, R.; Hinrichsen, O. Kinetics of Deactivation on $Cu/ZnO/Al_2O_3$ Methanol Synthesis Catalysts. *Appl. Catal. A* **2015**, *502*, 262–270. [CrossRef]
6. Bonura, G.; Khassin, A.A.; Yurieva, T.M.; Cannilla, C.; Frusteri, F.; Frusteri, L. Structure control on kinetics of copper oxides to methanol. *Catal. Today* **2020**, *342*, 39–45. [CrossRef]
7. Kattel, S.; Ramírez, P.J.; Chen, J.G.; Rodriguez, J.A.; Liu, P. Active sites for CO_2 hydrogenation to methanol on Cu/ZnO catalysts. *Science* **2017**, *355*, 1296–1299. [CrossRef]
8. Behrens, M.; Studt, F.; Kasatkin, I.; Kuhl, S.; Havecker, M.; Abild-Pedersen, F.; Zander, S.; Girgsdies, F.; Kurr, P.; Kniep, B.L.; et al. The Active Site of Methanol Synthesis over $Cu/ZnO/Al_2O_3$ Industrial Catalysts. *Science* **2012**, *336*, 893–897. [CrossRef]
9. Ghosh, S.; Uday, V.; Giri, A.; Srinivas, S. Biogas to methanol: A comparison of conversion processes involving direct carbon dioxide hydrogenation and via reverse water gas shift reaction. *J. Clean. Prod.* **2019**, *217*, 615–626. [CrossRef]
10. Kondrat, S.A.; Smith, P.J.; Carter, J.H.; Hayward, J.S.; Pudge, G.J.; Shaw, G.; Spencer, M.S.; Bartley, J.K.; Taylor, S.H.; Hutchings, G.J. The effect of sodium species on methanol synthesis and water-gas shift Cu/ZnO catalysts: Utilising high purity zincian georgeite. *Faraday Discuss.* **2017**, *197*, 287–307. [CrossRef]
11. Behrens, M. Meso- and nano-structuring of industrial $Cu/ZnO/(Al_2O_3)$ catalysts. *J. Catal.* **2009**, *267*, 24–29. [CrossRef]
12. Kühl, S.; Tarasov, A.; Zander, S.; Kasatkin, I.; Behrens, M. Cu-Based Catalyst Resulting from a Cu, Zn, Al Hydrotalcite-Like Compound: A Microstructural, Thermoanalytical, and In Situ XAS Study. *Chem. Eur. J.* **2014**, *20*, 3782–3792. [CrossRef] [PubMed]
13. Mota, N.; Guil-Lopez, R.; Pawelec, B.G.; Fierro, J.L.G.; Navarro, R.M. Highly active Cu/ZnO-Al catalyst for methanol synthesis: Effect of aging on its structure and activity. *RSC Adv.* **2018**, *8*, 20619–20629. [CrossRef]
14. Höppener, R.H.; Doesburg, E.B.M.; Scholten, J.J.F. Preparation and characterization of stable copper/zinc oxide/alumina catalysts for methanol synthesis. *Appl. Catal.* **1986**, *25*, 109–119. [CrossRef]
15. Fujita, S.I.; Satriyo, A.M.; Shen, G.C.; Takezawa, N. Mechanism of the formation of precursors for the Cu/ZnO methanol synthesis catalysts by a co-precipitation method. *Catal. Lett.* **1995**, *34*, 85–92. [CrossRef]

16. Anton, J.; Nebel, J.; Song, H.; Froese, C.; Weide, P.; Ruland, H.; Muhler, M.; Kaluza, S. The effect of sodium on the structure–activity relationships of cobalt-modified Cu/ZnO/Al_2O_3 catalysts applied in the hydrogenation of carbon monoxide to higher alcohols. *J. Catal.* **2016**, *335*, 175–186. [CrossRef]
17. Prieto, G.; de Jong, K.P.; de Jongh, P.E. Towards "greener" catalyst manufacture: Reduction of wastewater from the preparation of Cu/ZnO/Al_2O_3 methanol synthesis catalysts. *Catal. Today* **2013**, *215*, 142–151. [CrossRef]
18. Jeong, C.; Kim, T.; Kim, J.; Suh, Y.W. Use of tetraethylammoium bicarbonate as a precipitation agent on the preparation of co-precipitated Cu/ZnO catalysts. *Appl. Catal. A Gen.* **2017**, *541*, 35–41. [CrossRef]
19. Zuo, Y.Z.; An, X.; Han, M.H.; Wang, J.F.; Wang, D.Z.; Jin, Y. Effect of residual sodium on the catalytic activity and stability of Cu-based methanol synthesis catalyst. *Chin. J. Catal.* **2008**, *29*, 1266–1270.
20. Jun, K.W.; Shen, W.J.; Rao, K.S.R.; Lee, K.W. Residual sodium effect on the catalytic activity of Cu/ZnO/Al_2O_3 in methanol synthesis from CO_2 hydrogenation. *Appl. Catal. A Gen.* **1998**, *174*, 231–238. [CrossRef]
21. Suh, Y.W.; Rhee, H.K. Optimum Washing Conditions for the Preparation of Cu/ZnO/ZrO_2 for Methanol Synthesis from CO Hydrogenation: Effects of Residual Sodium. *Korean J. Chem. Eng.* **2002**, *19*, 17–19. [CrossRef]
22. Gimenez, P.; Fereres, S. Effect of Heating Rates and Composition on the Thermal Decomposition of Nitrate Based Molten Salts. *Energy Procedia* **2015**, *69*, 654–662. [CrossRef]
23. Millar, G.J.; Holm, I.H.; Uwins, P.J.; Drennan, J.J. Characterization of precursors to methanol synthesis catalysts Cu/ZnO system. *Chem. Soc. Faraday Trans.* **1998**, *94*, 593–600. [CrossRef]
24. Frost, R.L.; Locke, A.J.; Hales, M.C.; Martens, W.N. Thermal stability of synthetic aurichalcite implications for making mixed metal oxides for use as catalysts. *J. Therm. Anal. Calorim.* **2008**, *94*, 203–208. [CrossRef]
25. Schumann, J.; Tarasov, S.; Thomas, N.; Schlögl, R.; Behrens, M. Cu,Zn-based catalysts for methanol synthesis: On the effect of calcination conditions and the part of residual carbonates. *Appl. Catal. A Gen.* **2015**, *516*, 117–126. [CrossRef]
26. Bems, B.; Schur, M.; Dassenoy, A.; Junkes, H.; Herein, D.; Schlögl, R. Relations between Synthesis and Microstructural Properties of Copper/Zinc Hydroxycarbonates. *Chem. Europ. J.* **2003**, *9*, 2039–2052. [CrossRef]
27. Dal Pozzo, A.; Armutlulu, A.; Rekhtina, M.; Abdala, P.M.; Müller, C.R. CO_2 Uptake and Cyclic Stability of MgO-Based CO_2 Sorbents Promoted with Alkali Metal Nitrates and Their Eutectic Mixtures. *ACS Appl. Energy Mater.* **2019**, *2*, 1295–1307. [CrossRef]
28. Zhang, K.; Li, X.S.; Li, W.Z.; Rohatgi, A.; Duan, Y.; Singh, P.; Li, L.; King, D.L. Phase Transfer-Catalyzed Fast CO_2 Absorption by MgO-Based Absorbents with High Cycling Capacity. *Adv. Mater. Interfaces* **2014**, *1*, 1400030. [CrossRef]
29. Rekhtina, M.; Dal Pozzo, A.; Stoian, D.; Armutlulu, A.; Donat, F.; Blanco, M.V.; Wang, Z.-J.; Willinger, M.G.; Fedorov, A.; Abdala, P.M.; et al. Effect of molten sodium nitrate on the decomposition pathways of hydrated magnesium hydroxycarbonate to magnesium oxide probed by in situ total scattering. *Nanoscale* **2020**, *12*, 16462–16473. [CrossRef]
30. Jo, S.-I.; An, Y.-N.; Kim, K.-Y.; Choi, S.-Y.; Kwak, J.-S.; Oh, K.-R.; Kwon, Y.U. Mechanisms of absorption and desorption of CO_2 by molten $NaNO_3$-promoted MgO. *Phys. Chem. Chem. Phys.* **2017**, *19*, 6224–6232. [CrossRef]
31. Harada, T.; Simeon, F.; Hamad, E.Z. Hatton, Alkali Metal Nitrate-Promoted High-Capacity MgO Adsorbents for Regenerable CO_2 Capture at Moderate Temperatures. *Chem. Mater.* **2015**, *27*, 1943–1947. [CrossRef]
32. Tarasov, A.; Schumann, J.; Thomas, N.; Behrens, M. Thermokinetic investigation of binary Cu/Zn hydroxycarbonates as precursors for Cu/ZnO catalysts. *Termochim. Acta* **2014**, *591*, 1–9. [CrossRef]
33. Fujita, S.; Moribe, S.; Kanamori, Y.; Kakudate, M.; Tazekawa, N. Preparation of a coprecipitated Cu/ZnO catalyst for the methanol synthesis from CO_2–Effects of the calcination and reduction conditions on the catalytic performance. *Appl. Catal. A Gen.* **2001**, *207*, 121–128. [CrossRef]
34. Sloczynski, J.; Grabowski, R.; Kozlowska, A.; Olszewski, P.K.; Stoch, J. Reduction kinetics of CuO in CuO/ZnO/ZrO_2 systems. *Phys. Chem. Chem. Phys.* **2003**, *5*, 4631–4640. [CrossRef]
35. Gao, P.; Li, F.; Xiao, F.K.; Zhao, N.; Sun, N.N.; Wei, W.; Zhong, L.S.; Sun, Y.H. Preparation and activity of Cu/Zn/Al/Zr catalysts via hydrotalcite-containing precursors for methanol synthesis from CO_2 hydrogenation. *Catal. Sci. Technol.* **2012**, *2*, 1447–1454. [CrossRef]
36. Shimokawabe, M.; Asakawa, H.; Takezawa, N. Characterization of copper/zirconia catalysts prepared by an impregnation method. *Appl. Catal.* **1990**, *59*, 45–58. [CrossRef]

37. Breen, J.P.; Ross, J.R. Methanol reforming for fuel-cell applications: Development of zirconia-containing Cu–Zn–Al catalysts. *Catal. Today* **1999**, *51*, 521–533. [CrossRef]
38. Yuvaraj, S.; Fan-Yuan, L.; Tsong-Huei, C.; Chuin-Tih, Y. Thermal Decomposition of Metal Nitrates in Air and Hydrogen Environments. *J. Phys. Chem. B* **2003**, *107*, 1044–1047. [CrossRef]
39. Ressler, T.; Kneip, B.L.; Kasatkin, I.; Schlögl, R. The Microstructure of Copper Zinc Oxide Catalysts: Bridging the Materials Gap. *Angew. Chem. Int. Ed.* **2003**, *44*, 4704–4707. [CrossRef]
40. Prašnikar, A.; Pavlišič, A.; Ruiz-Zepeda, F.; Kovač, J.; Likozar, B. Mechanisms of Copper-Based Catalyst Deactivation during CO_2 Reduction to Methanol. *Ind. Eng. Chem. Res.* **2019**, *58*, 13021–13029. [CrossRef]
41. Fichtl, M.B.; Schumann, J.; Jacobsen, N.C.; Behrens, M.; Schlögl, R.; Muhler, M.; Hinrichsen, O. Counting of Oxygen Defects versus Metal Surface Sites in Methanol Synthesis Catalysts by Different Probe Molecules. *Angew. Chem. Int. Ed.* **2014**, *53*, 7043–7047. [CrossRef] [PubMed]
42. Nakamura, J.; Choi, Y.; Fujitani, T. On the Issue of the Active Site and the Role of ZnO in Cu/ZnO Methanol Synthesis Catalysts. *Top. Catal.* **2003**, *22*, 277–285. [CrossRef]
43. Lunkenbein, T.; Schuman, J.; Behrens, M.; Schlögl, R.; Willinger, M.G. Formation of a ZnO Overlayer in Industrial Cu/ZnO/Al_2O_3 Catalysts Induced by Strong Metal–Support Interactions. *Angew. Chem.* **2015**, *127*, 4627–4631. [CrossRef]
44. Schuman, J.; Lunkebein, T.; Tarasov, A.; Thomas, N.; Schlögl, R.; Behrens, M. Synthesis and Characterisation of a Highly Active Cu/ZnO:Al Catalyst. *ChemCatChem* **2014**, *6*, 2889–2897. [CrossRef]
45. Behrens, M.; Zander, S.; Kurr, P.; Jacobsen, N.; Senker, J.; Koch, G.; Ressler, T.; Fischer, R.W.; Schlögl, R. Performance Improvement of Nanocatalysts by Promoter-Induced Defects in the Support Material: Methanol Synthesis over Cu/ZnO:Al. *J. Am. Chem. Soc.* **2013**, *135*, 6061–6068. [CrossRef]
46. Bond, G.C.; Namijo, S.N. An improved procedure for estimating the metal surface area of supported copper catalysts. *J. Catal.* **1989**, *118*, 507–510. [CrossRef]